Cassini UVIS Observations of the Enceladus Auroral Footprint on Saturn in 2017

Wayne R. Pryor, Fabiola P. Magalhães, Laurent Lamy, Renée Prangé, Larry W. Esposito, Jacques Gustin, Abigail M. Rymer, Ali H. Sulaiman

The Planetary Science Journal, 5:20 (13pp), 2024 January https://doi.org/10.3847/PSJ/ad0cbc

Cassini UVIS Observations of the Enceladus Auroral Footprint on Saturn in 2017

Wayne R. Pryor[1,2], Fabiola P. Magalhães[3], Laurent Lamy[4,5], Renée Prangé[4], Larry W. Esposito[6], Jacques Gustin[7], Abigail M. Rymer[8], and Ali H. Sulaiman[9]
[1] Space Environment Technologies, LLC, 528 Palisades Drive, Ste 164, Pacific Palisades, CA 90272-2844, USA
[2] Central Arizona College, Science & Engineering Division, 8470 N. Overfield Road, Coolidge, AZ 85128, USA
[3] Independent Researcher, Florianopolis, SC, Brazil
[4] Laboratoire d'Etudes Spatiales et d'Instrumentation en Astrophysique, Observatoire de Paris, PSL, CNRS, Meudon, France
[5] Aix Marseille Université, CNRS, CNES, LAM, Marseille, France
[6] Laboratory for Atmospheric and Space Physics, University of Colorado at Boulder, Boulder, CO 80303, USA
[7] Independent Researcher, Liège, Belgium
[8] Johns Hopkins University, Applied Physics Laboratory, Laurel, MD 20723, USA
[9] School of Physics & Astronomy, University of Minnesota, Minneapolis, MN 55455, USA
Received 2023 June 6; revised 2023 November 4; accepted 2023 November 13; published 2024 January 24

Abstract

Ultraviolet Imaging Spectrograph (UVIS) observations show the Enceladus auroral footprint on Saturn on 2017 September 14, near the end of the Cassini mission. A series of Saturn north polar auroral images were obtained by slowly slewing the Cassini spacecraft at right angles to the UVIS long slit. The images were limb-fit to improve the spacecraft geometry. Enhanced extreme-ultraviolet 88–118 nm channel emissions due to electron impact on atomic and molecular hydrogen were seen in the expected location for the Enceladus auroral footprint on five successive images spanning almost 4 hr. Enhanced emissions were also seen in simultaneously obtained far-ultraviolet 111–165 nm images in at least two of these images, with the spectral signature expected for auroral emissions. While most Cassini UVIS auroral images do not show the Enceladus auroral footprint, these 2017 images support the earlier detection of an Enceladus-linked spot on Saturn in 2008 Cassini UVIS data.

Unified Astronomy Thesaurus concepts: Aurorae (2192); Planetary magnetospheres (997)

1. Introduction

The Cassini Ultraviolet Imaging Spectrograph (UVIS) instrument (Esposito et al. 2004) orbited Saturn from 2004 to 2017, providing a large set of spatial and spectral observations of auroral emissions in Saturn's atmosphere (e.g., Esposito et al. 2005; Grodent et al. 2011; Lamy et al. 2013; Gustin et al. 2017; Palmaerts et al. 2018; Pryor et al. 2019; Radioti et al. 2019; Bader et al. 2020). Here we focus on the search for UVIS auroral emissions on Saturn on magnetic field lines associated with its moon Enceladus, which has active geysers providing water-rich material to Saturn's magnetosphere (e.g., Hansen et al. 2006; Waite et al. 2006) with ongoing activity recently imaged by the James Webb Space Telescope in 2022 (Villanueva et al. 2023). Auroral footprint emissions on Saturn from its moons might be expected based on observations of satellite footprints in the Jupiter system associated with the moons Io, Europa, and Ganymede at near-infrared and far-ultraviolet (FUV) wavelengths (e.g., Connerney et al. 1993; Prangé et al. 1996, Clarke et al. 2002; Bonfond 2013; Bonfond et al. 2017; Mura et al. 2018).

Previous work found that three sequential Cassini UVIS Saturn north polar images from 2008 showed enhanced emission corresponding to the location of the auroral footprint of Saturn's moon Enceladus (Pryor & Rymer et al. 2011; Gustin et al. 2017; Magalhães et al. 2019). However, out of a set of thousands of Cassini UVIS auroral images obtained while orbiting Saturn, very few have contained any indication of the presence of footprint emissions, suggesting they may usually be very weak or absent. The Enceladus footprint is also too faint to be seen with the Hubble Space Telescope (HST) Space Telescope Imaging Spectrograph (STIS) or Advanced Camera for Surveys (ACS) (Wannawichian et al. 2008; Lamy et al. 2018).

Cassini made a long series of high-inclination orbits of Saturn at the end of the mission in 2017, providing a large set of auroral images with favorable viewing geometries for studying the polar auroras. We report here on a set of UVIS observations made on 2017 September 13–14. Five sequential images from September 14 obtained from 05:54 to 09:53, with auroral zone crossings spanning about 3 hr and 40 minutes, show evidence for enhanced emission in the expected location of the Enceladus auroral footprint in the extreme-ultraviolet (EUV) channel, and the last two images also show enhanced emissions in the same location in the FUV channel.

2. Observations and Data Analysis

The Cassini UVIS instrument contained two optically separated spectrograph channels, covering the EUV (56.3–118.2 nm) and the FUV (111.5–191.2 nm). For the observations on 2017 September 13–14, the EUV channel with its 1024 spectral × 64 spatial pixel detector was observing with its 2 mrad wide by 60 mrad long slit. The FUV channel with its 1024 spectral × 64 spatial pixel detector was observing with a slightly narrower 1.5 mrad by 60 mrad slit. These fields of view partially overlap. Both channels were recording a spectral image every 16 s. Both EUV and FUV data will be presented in this paper.

The Cassini UVIS team created Portable Document Format (PDF) books of auroral images formed by slowly slewing the UVIS slit across Saturn. These "auroral books" are archived with the Planetary Data System[10] to help users identify data

[10] https://atmos.nmsu.edu/data_and_services/atmospheres_data/Cassini/CASSINIUVIS/UVIS-11A//

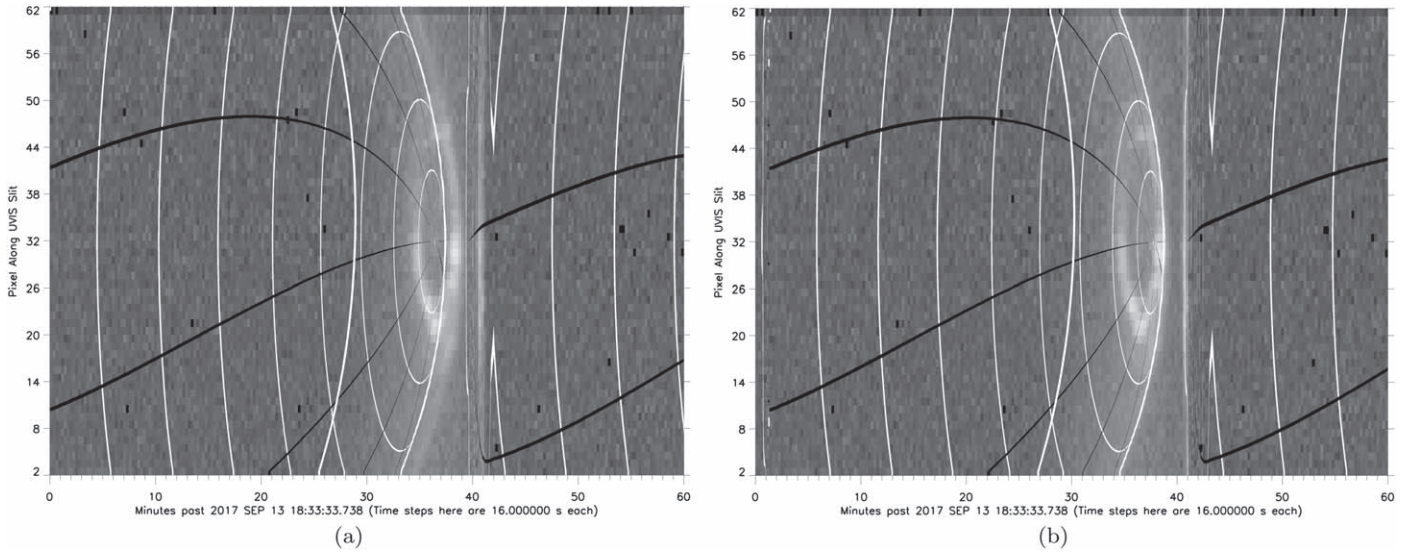

Figure 1. (a) A sample page from the archived UVIS book of auroral images from 2017 September 13, modified to add a calculated planetary limb using the standard pointing kernels. The file was labeled *FUV*2017_256_18_32_28_*UVIS*_293*SA_AURSLEW*001_*PRIME* and was obtained from a sub-spacecraft latitude of 16.°63N, an altitude above Saturn of 16.8R_s, and a phase angle with respect to Saturn's center of 136.°5. In this case, the FUV wavelengths from 111 to 165 nm that may show atomic hydrogen Lyα and molecular hydrogen band emissions are included. Time is on the horizontal axis, and the 60 spatial pixels along the UVIS FUV slit are displayed vertically. White latitude lines are drawn every 10° and black longitude lines every 30°. In this case, the initial geometric limb overlay formed from Cassini geometry kernels is a poor fit to the limb and auroral emissions. (b) In this case, the geometric overlay has been shifted by 80 s (five 16 s time steps later) to manually limb-fit the observations.

cubes of interest for further study. Geometric overlays were included with these images in the auroral books. Because the auroras occur in the upper atmosphere (Gérard et al. 2009), the nominal Saturn radius used in the overlays has been increased by 1100 km from the values used in the JPL SPICE system geometry kernels. For most Saturn orbits, the planetary limb appears to be in the correct place with respect to the geometric overlays visually. However, in the case of the Rev 293 observations discussed further below, there is a systematic offset: the overlays formed from the JPL-provided geometry kernels need to be shifted by five time steps (80 s) to achieve apparent agreement between the location of the planetary emissions at the planet's limb and the location of the geometric limb. Figure 1 shows a sample UVIS FUV image before and after the time shift to illustrate the limb-fitting procedure. In these images, the UVIS slit swept across the night side of Saturn, crossed the terminator (overlaid as a thick white arc cutting across latitude lines), and crossed the solar-illuminated north polar auroral zone from minutes 35–38, forming an auroral image, crossed the planetary limb (thin white arc), and then viewed off-limb. The sliver of emission near minute 41 is a rapid "flyback slew" across Saturn between successive slowly formed auroral images. The time-shifted image shown in Figure 1(b) better fits both the limb in the main image and the limb-crossing on the flyback slew.

As was done in our initial paper on the Enceladus footprint (Pryor & Rymer et al. 2011), a search box was placed on the geometric overlays at the expected location of the Enceladus magnetic footprint. The search box was centered on the sub-Enceladus longitude with a width in longitude of 12° and at a planetocentric latitude of 64.°5N with a height in latitude of 9°, based on models of Saturn's magnetic field. After browsing a large set of images in these auroral books modified for possible Enceladus footprint detections, a sequence of several of these geometry-adjusted images from 2017 September 14 was spotted independently by two of the authors as having additional emission inside the search boxes that appeared to move slowly with Enceladus (32.9 hr orbital period) and not, for example, with Saturn (~10.6 hr rotation period). The observing sequence presented here, labeled UVIS_293SA_AURSLEW001_PRIME, was executed from 2017-256T18:30 to 2017-257T13:20 (September 13–14) and produced 22 images formed by slow sweeps of the long UVIS slits across Saturn from sub-spacecraft latitudes of 16.°6–23.°3N, spacecraft phase angles of 136.°5–130.°0, and spacecraft ranges of 16.8–12.8 R_s, where one Saturn radius (R_s) = 58,232 km. Figure 2 shows a sample EUV image, Image 18, showing summed data from the long-wavelength half of the EUV detector (88–118 nm) where H_2-band molecular emission is expected and enhanced emission inside the search box post-midnight. The excess emission shows up mostly in a single spatial pixel for several time steps, which matches the expected behavior for the 2 mrad wide slit moving over a nearly point-source emission, as discussed further below. Figure 2 also shows the corresponding FUV image obtained at the same time with a narrower 1.5 mrad slit. In this case, the spectral range used was 111–165 nm, excluding Lyα emission from 120 to 123 nm, because diffuse Lyα dayglow reduces the contrast of any spots of auroral emission. This choice also rejects bright longer-wavelength FUV data from 165 to 191 nm due to scattered sunlight (Rayleigh scattering from gas molecules and scattering by aerosols), as discussed by Gustin et al. (2010) and Pryor et al. (2019). The resulting FUV image is noisier than the EUV image and excess emission appears in two spatial pixels. Real point sources like calibration stars can show up in two spatial pixels in a spectrally summed UVIS FUV image because the instrument places a slightly tilted spectral image on the FUV detector.

The spatial resolution of these observations depends on range. For example, near the middle of the observation, from a range of ~800,000 km, an EUV spatial pixel, 1 mrad tall and 2 mrad wide given the slit choice, neglecting slit motion,

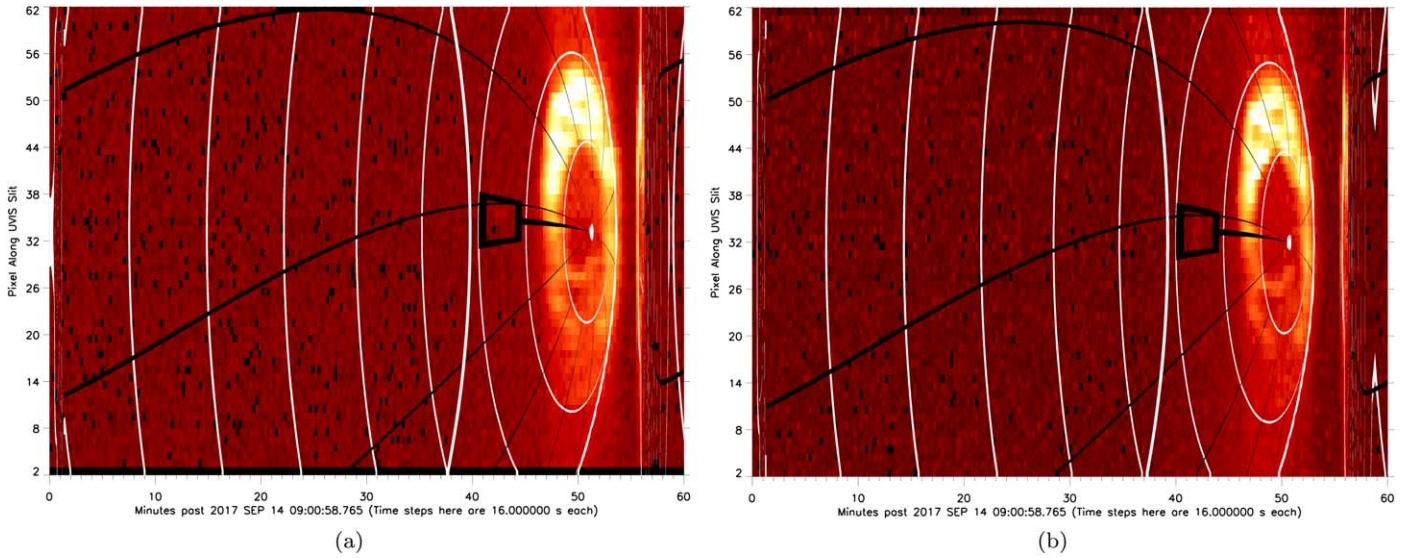

Figure 2. (a) EUV image 18 of the 22-image UVIS observing sequence with a limb-fit geometric overlay. The file was labeled *EUV*2017_257_08_59_53_*UVIS*_293*SA*_*AURSLEW*001_*PRIME*, was obtained from a sub-spacecraft latitude of 22.°3N, an altitude above Saturn of 13.4R_S, and a phase angle of 131.°0. Spectrally summed 88–118 nm data are shown. The northern auroral oval is visible at the right. The black search box indicates the expected location of the Enceladus auroral footprint. The terminator is the thicker white line left of the search box, which was in sunlight. (b) The corresponding FUV image, from file *FUV*2017_257_08_59_53_*UVIS*_293*SA*_*AURSLEW*001_*PRIME*, shows spectrally summed 111–165 nm data, excluding H Lyα (120–123 nm) data and and the bulk of the reflected sunlight (165–191 nm) emissions.

observed 800 km × 1600 km on the sky. An FUV spatial pixel, 1 mrad tall and 1.5 mrad wide, observed a slightly smaller patch of sky, 800 km × 1200 km. At the selected slew rate of 0.03 mrad s^{-1}, and an integration time of 16 s, the slit moved 0.48 mrad in an integration time, making the observed region in that spatial pixel for that integration period 0.48 mrad larger in the cross-slit direction: 800 km × 2000 km for EUV and 800 km × 1600 km for FUV. Since a single integration moves the slit 0.48 mrad across a point source, it takes roughly three integration periods for a point source to cross the 1.5 mrad wide FUV slit, giving an oversampling by about a factor of 3. In other words, a real point source should appear in this FUV data set in roughly three successive integration periods. The wider 2 mrad EUV slit will take four integration periods to cross a point source. Because the spectral image of a point source on the detector is slightly tilted with respect to the UVIS FUV detector rows, a point source is usually imaged onto two adjacent spatial pixels. This means that a good test for the reality of a weak point source of emission in these UVIS FUV images is to search for bright features in two adjacent spatial pixels persisting for three 16 s time steps. In the EUV, auroral H_2-band spectral emission is only seen on the long-wavelength half of the detector, making it more likely for a point source to be imaged into a single spatial pixel, probably in four 16 s time steps. Each image in UVIS_293SA_AURSLEW001_PRIME took about 20 minutes to obtain, with the 1024 spectral channels rebinned evenly into 64 spectral channels in the onboard UVIS microprocessor, with only the central 60 spatial pixels returned to Earth for telemetry reasons. These images are stored as data cubes, with spectral, spatial, and time dimensions. Most of the auroral images obtained during the Cassini mission used a shorter 8 s integration period, making this unusual 16 s observation sequence more favorable for detecting faint emissions. Figures 3 and 4 show five polar-projected images (Images 14–18) from the EUV detector (88–118 nm selected) and the simultaneously obtained Images 14–18 from the FUV detector (130–165 nm selected), taken from the longer 22-image observing sequence. Images before and after these are harder to search, as the search box is approaching the bright limb in Lyα and because along-slit scattered light from the auroral zone is adding to the apparent signal. Enhanced emission in the red search box is more obvious in the EUV images, which have less residual scattered light and dayglow than the corresponding FUV images. The search box remained in sunlight throughout the observing sequence, and the terminator is displayed as a curved white line on the image. Midnight is to the right, and the detections spanned a time interval of about 3 hr and 40 minutes. The five EUV images selected do have indications of enhanced emission in the Enceladus footprint search box both pre-midnight and near midnight. Only the last two FUV images (shown in Figure 4) distinctly show a visible Enceladus footprint in the search box.

Next we tabulated details about these 10 images. The higher-contrast EUV images were better suited for determining the location of the emission relative to the expected sub-Enceladus footprint (Table 1). We found that using the brightest pixel in the search box led to finding the Enceladus footprint at the expected location near 64.°5N and the sub-Enceladus longitude within our measurement uncertainties, which come from limb-fitting errors and the finite size of an EUV observing pixel (1 mrad along the slit and 2 mrad across the slit) and its expected cross-slit motion of 0.48 mrad in 16 s. The intrinsic pixel size and its motion on Saturn during each 16 s integration were used to set the geometric error bars shown in the table. To investigate the amount of excess emission, we formed a background estimated brightness near the brightest pixel in the search box by averaging five time steps of data using adjacent spatial pixels on each side, two spatial sectors away from the brightest pixel. Comparing the measured peak signals to the background estimates leads to Enceladus-related excess EUV emissions of ∼0.1–0.2 kR. Next we looked at the statistical significance of the detections based on just the brightest pixel in each search box and found σ values for the detections ranging from 2.8σ to 7.2σ. We also looked at three-pixel

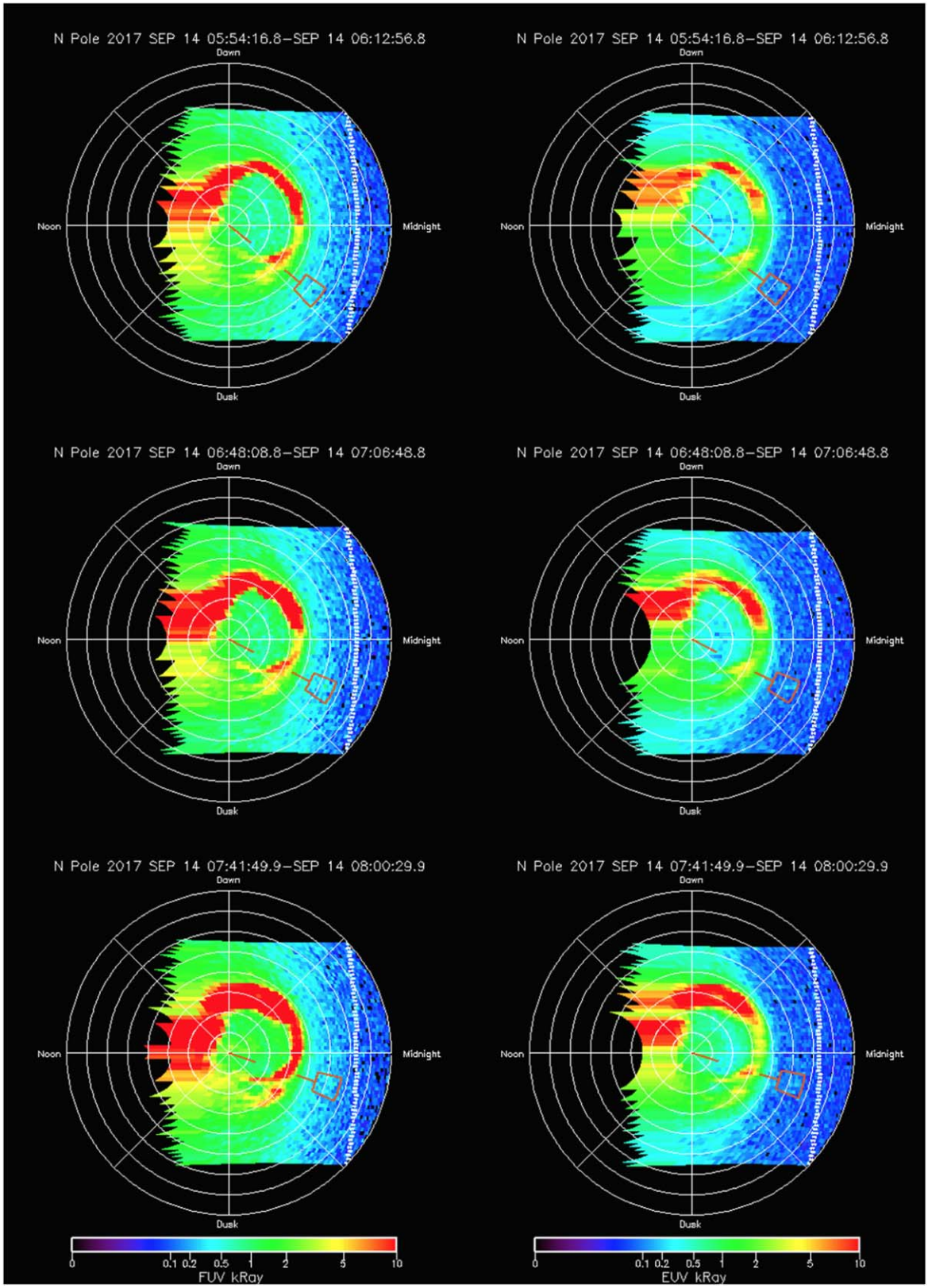

Figure 3. Left column: FUV (130–165 nm) polar-projected Images 14–16 of the 22-image set obtained on 2017 September 13–14. The times shown are the start and end of each observation. Right column: corresponding EUV (88–118 nm) polar-projected Images 14–16 of the 22-image set obtained on 2017 September 13–14. In this case, the EUV footprints are obvious and the FUV footprints, if present, are obscured by the background.

averages, where we took the brightest pixel as the center of the three time steps of interest, since we expect excess emission in three or four time steps if the spacecraft slews across a point source of emission. This leads to slightly lower excess emission of ∼0.060–0.160 kR and similar σ values for the detections of 2.8σ–8.4σ.

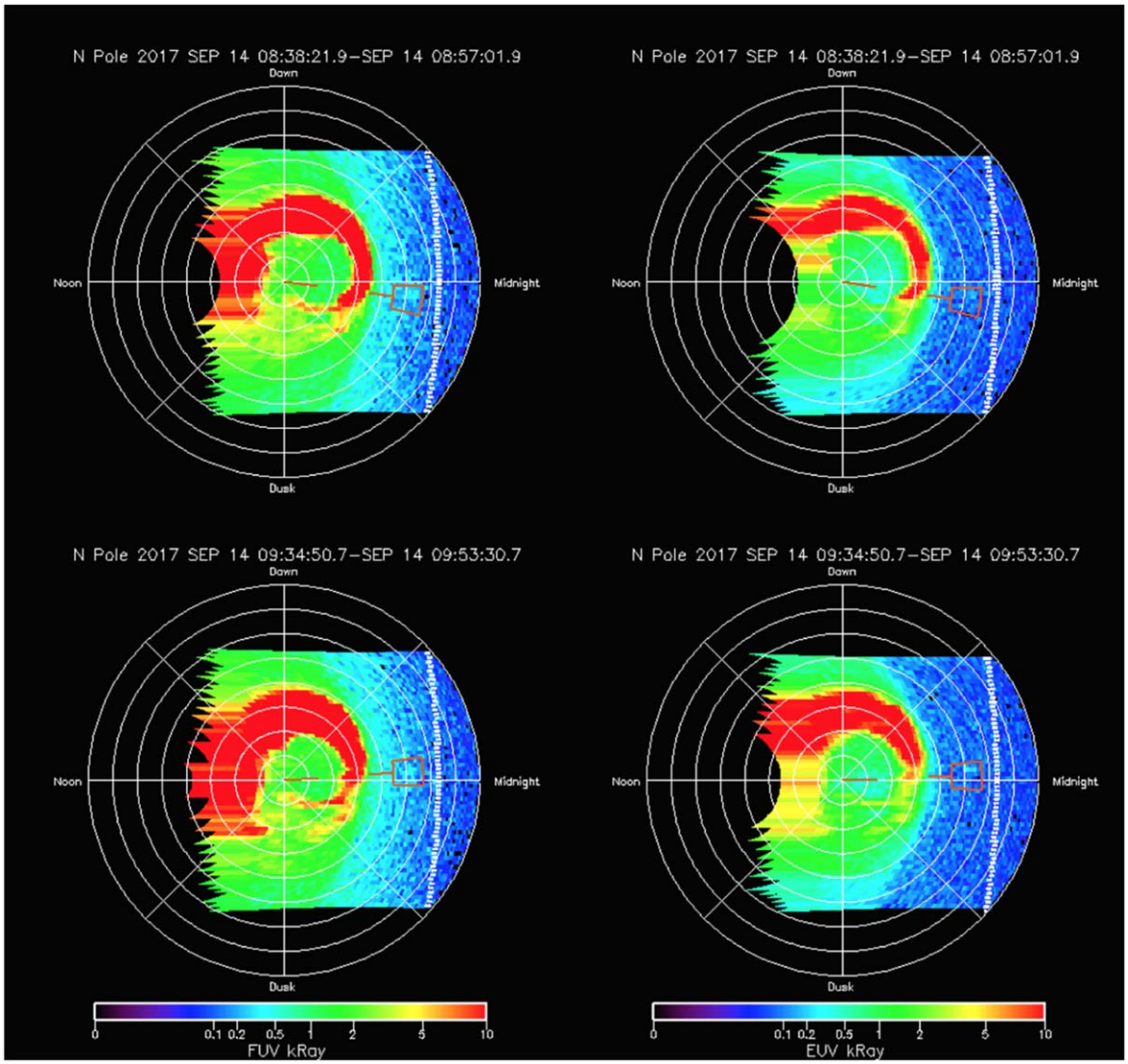

Figure 4. Left column: FUV (130–165 nm) polar-projected Images 17–18 of the 22-image set obtained on 2017 September 13–14. The times shown are the start and end of each observation. Right column: corresponding EUV (88–118 nm) polar-projected Images 17–18 of the 22-image set obtained on 2017 September 13–14. In this case, both the EUV and FUV footprints are obvious in the data.

In Table 2, we looked at the brightness and significance of the corresponding FUV spot images. Because of slight boresight offsets between the two instruments, a point source like a star that has a spectrum centered on FUV spatial pixel 34, for example, will have a spectrum centered on EUV spatial pixel 35 (McClintock 2002). For three of the five spots, the brightest FUV pixel in the search box was one spatial pixel lower than for the brightest EUV pixel, as expected based on the boresight calibration. We chose to look at first the corresponding FUV pixel to the observed EUV brightest pixel, then at three-pixel averages (the averages over three time steps). We also looked at two spectral ranges, 111–165 nm, which captures auroral H_2-band and H Lyα emission, as well as widespread Lyα dayglow, and also specifically at 130–165 nm data, which excludes the widespread Lyα emission. The 130–165 nm images made the FUV spots a bit easier to see. A key point in the tabulated results is the declining background level found in the search boxes as the image sequence progressed. This is because as the expected Enceladus footprint location moved toward midnight, it moved closer to the terminator, where the expected dayglow emissions, such as H Lyα and H_2-band emissions (Gustin et al. 2010), are greatly reduced. It also moved away from any along-slit scattered light from auroral emissions or from long-wavelength reflected sunlight. Examining the various cases presented in Table 2, it appears that only the last two images, Image 17 and Image 18, had small enough backgrounds for the FUV emission to be seen clearly, with detection significance values of σ ranging from 1.55 to 6.17, depending on which case is considered. For Images 17 and 18, we can add the three-pixel averages from the EUV and FUV together to obtain an estimate of emission from 87 to 165 nm of 0.22 ± 0.13 kR for Image 17 and 0.52 ± 0.12 kR for Image 18. Even viewing the same spot, there may be a time offset between EUV and FUV as the fields of view only partially overlap, with their centers offset by 1 mrad. The leading edge of the 1.5 mrad wide FUV slit, which is offset by 0.75 mrad from the leading edge of the 2.0 mrad wide EUV slit, reached the spot first by about 0.75 mrad/(0.03 mrad s^{-1} slew rate) = 25 s, or slightly longer than one 16 s integration period, so the FUV might be expected to brighten first—that is, at a smaller time step. Summing the two channels should be done with the understanding that the slits are not identical in width and only partially overlap. The fact that the two channels are optically independent

Table 1
Detected Enceladus Spots in 2017 September 14 Cassini UVIS EUV Data

Image	Image Times	Slant Range in R_s	Sub-Spacecraft Latitude	EUV Brightest Pixel Latitude	EUV Brightest Pixel Longitude Offset	EUV Brightest Pixel Coordinates (Spatial Sector, Time Step)	EUV Brightest Pixel (kR)	EUV Background Estimate (kR)	EUV Brightest Pixel Detection Significance in σ	EUV Brightest Pixel Excess Emission (kR)
14	05:54:16.8– 06: 12: 56.8	14.6	20.°9N	$63.°8 \pm 1.°7$N	$-2.°7 \pm 3.°4$	15, 149 15, 148 − 150	0.242 ± 0.063 0.138 ± 0.027	0.082 ± 0.012 0.082 ± 0.012	4.45 2.82	0.160 ± 0.064 0.056 ± 0.030
15	06:48:08.8– 07: 06: 48.8	14.3	21.°3N	$64.°6 \pm 1.°7$N	$+0.°4 \pm 3.°0$	18, 352 18, 351 − 353	0.299 ± 0.072 0.197 ± 0.033	0.092 ± 0.012 0.092 ± 0.012	5.02 4.57	0.207 ± 0.073 0.105 ± 0.035
16	07:41:49.9– 08: 00: 29.9	14.0	21.°7N	$64.°1 \pm 1.°7$N	$+0.°1 \pm 2.°2$	22, 153 22, 152 − 154	0.215 ± 0.058 0.179 ± 0.031	0.115 ± 0.014 0.115 ± 0.014	2.79 2.94	0.100 ± 0.060 0.064 ± 0.034
17	08:38:21.9– 08: 57: 01.9	13.8	22.°2N	$64.°0 \pm 1.°6$N	$-0.°1 \pm 1.°5$	27, 364 27, 363 − 365	0.213 ± 0.059 0.175 ± 0.032	0.099 ± 0.013 0.099 ± 0.013	2.92 3.07	0.114 ± 0.060 0.076 ± 0.034
18	09:34:50.7– 09: 53: 30.7	13.5	22.°6N	$65.°2 \pm 1.°6$N	$-1.°8 \pm 1.°3$	33, 161 33, 160 − 162	0.295 ± 0.069 0.225 ± 0.035	0.068 ± 0.011 0.068 ± 0.011	7.20 8.41	0.227 ± 0.069 0.157 ± 0.037

Note. The "brightest pixel" refers to the search box on the image only, which covers $64.°5 \pm 3°$N and sub-Enceladus longitude $\pm 6°$. A negative longitude offset means the brightest pixel is offset from the search box center in the direction of planetary rotation. "EUV" here refers to EUV channel 87–118 nm data. The second row for each image involves averages over three time steps.

Table 2
Enceladus Spots in the 2017 September 14 Cassini UVIS FUV Data

Image	Image Times	FUV Selected Pixels Coordinates (Spatial Sector, Time Step)	FUV Selected Pixels (kR)	FUV Background Estimate (kR)	FUV Selected Pixels Detection Significance in σ	FUV Selected Pixels Excess Emission (kR)
14	05:54:16.8–06: 12: 56.8	14, 149	0.883 ± 0.178	0.970 ± 0.061	-0.055	-0.087 ± 0.188
		14, 148–150	1.139 ± 0.138	0.970 ± 0.061	-0.75	0.170 ± 0.151
		(14, 149)	(0.352 ± 0.111)	(0.338 ± 0.033)	(-0.14)	(0.013 ± 0.116)
		(14, 148–150)	(0.338 ± 0.062)	(0.338 ± 0.033)	(-0.34)	(-0.001 ± 0.070)
15	06:48:08.8–07: 06: 48.8	17, 352	1.000 ± 0.259	0.936 ± 0.067	-1.10	0.064 ± 0.268
		17, 351–353	0.819 ± 0.117	0.936 ± 0.067	-1.38	-0.117 ± 0.135
		(17, 352)	(0.321 ± 0.118)	(0.314 ± 0.035)	(-0.24)	(0.007 ± 0.123)
		(17, 351–353)	(0.338 ± 0.069)	(0.314 ± 0.035)	(-0.06)	(0.024 ± 0.077)
16	07:41:49.9–08: 00: 29.9	21, 153	0.604 ± 0.143	0.785 ± 0.052	-1.01	-0.181 ± 0.153
		21, 152–154	0.793 ± 0.101	0.785 ± 0.052	-0.81	0.008 ± 0.114
		(21, 153)	(0.228 ± 0.084)	(0.344 ± 0.033)	(-1.07)	(-0.116 ± 0.091)
		(21, 152–154)	(0.250 ± 0.050)	(0.344 ± 0.033)	(-1.37)	(-0.093 ± 0.060)
17	08:38:21.9–08: 57: 01.9	26, 364	0.762 ± 0.172	0.762 ± 0.065	1.55	0.000 ± 0.184
		26, 363–365	0.905 ± 0.103	0.762 ± 0.065	5.51	0.144 ± 0.122
		(26, 364)	(0.314 ± 0.104)	(0.229 ± 0.032)	(1.88)	(0.085 ± 0.109)
		(26, 363–365)	(0.335 ± 0.059)	(0.229 ± 0.032)	(4.44)	(0.106 ± 0.067)
18	09:34:50.7–09: 53: 30.7	32, 161	0.988 ± 0.161	0.587 ± 0.047	5.55	0.401 ± 0.168
		32, 160–162	0.949 ± 0.100	0.587 ± 0.047	6.17	0.361 ± 0.111
		(32, 161)	(0.577 ± 0.119)	(0.242 ± 0.028)	(5.93)	(0.335 ± 0.123)
		(32, 160–162)	(0.307 ± 0.051)	(0.242 ± 0.028)	(3.05)	(0.645 ± 0.058)

Note. A "selected pixel" refers to the 111–165 nm data from the FUV pixel that best corresponds with the EUV pixel selected in Table 1. The data in parentheses refer to the higher-contrast 130–165 nm data that exclude the Lyα 121.6 nm data. The second and fourth rows for each image refer to averages over three time steps. Negative σ values should be interpreted as nondetections of an FUV footprint in Images 14, 15, and 16.

increases our confidence in these detections of spots seen in both channels.

2.1. Data Analysis Part 2

In parallel to the abovementioned efforts, the Cassini UVIS team in Meudon independently processed the same UVIS data set with similar steps (including the pointing correction) and additional ones. The primary goal was to construct individual (level 2) data files for each slewing of the (northern or southern) auroral region to make them accessible through the Auroral Planetary Imaging and Spectroscopy (APIS) service (Lamy et al. 2015, 2021) and to build up higher-level (level 3) data including maps—either in the original UVIS field of view or projected into a polar view of auroral (only) H_2 and H Lyα emissions and of the normalized Color Ratio (CR) proxy (the ratio of the H_2 brightness integrated over the 123–130 and 144–166 nm bands) and the Brightness Ratio (BR) one (the ratio of the H Lyα brightness over the total H_2 one; for details, see Lamy et al. 2013, especially the Appendix; also see Tao et al. 2014; Gustin et al. 2017). For each UVIS FUV data file, the average long-wavelength solar reflected contribution was specifically determined from nonauroral illuminated spatial pixels and then removed in each spatial pixel of the file, yielding solar-clean spectra. It was then straightforward to derive the total H_2 brightness over 80–160 nm (corrected for absorption) with an improved signal-to-noise ratio, the total H Lyα brightness (corrected for absorption and H_2 underlying contribution), and the associated values of CR and BR.

By conducting a survey of the UVIS data set, we could track in individual observations (i.e., without having to average them) the Enceladus footprint already reported in the UVIS measurements of 2008 by Pryor & Rymer et al. (2011). Figure 5 shows four maps of the above described observables for the UVIS FUV processed observation of 2008 August 26 at 00:53:35 (Magalhães et al. 2019). In addition to the H_2 spot in the white search box (top left) reported by Pryor et al. (2011), we could clearly identify the H Lyα emission of the same spot, as well as the main auroral oval (top right). CR and BR complementary proxies were shown by Gustin et al. (2017) to be sensitive to primary electrons of $\geqslant$10 and $\leqslant$10 keV kinetic energies, respectively. The Enceladus spot was more visible in the BR map (bottom right) than in the CR one (bottom left), as was the equatorward portion of the main auroral oval. Additionally, we also newly identified the footprint in the UVIS FUV measurements taken on 2017 September 13–14. Their detailed analysis is the purpose of the next section.

3. Discussion

The five sequential images from 2017 presented here together with the three sequential images from 2008 presented before in Pryor & Rymer et al. (2011) constitute strong evidence that there is at least occasionally an Enceladus-related auroral footprint on Saturn. As mentioned before, thousands of images were searched to find these eight images. There are hints of excess emission in the correct location in other individual images, but without a series of images moving with

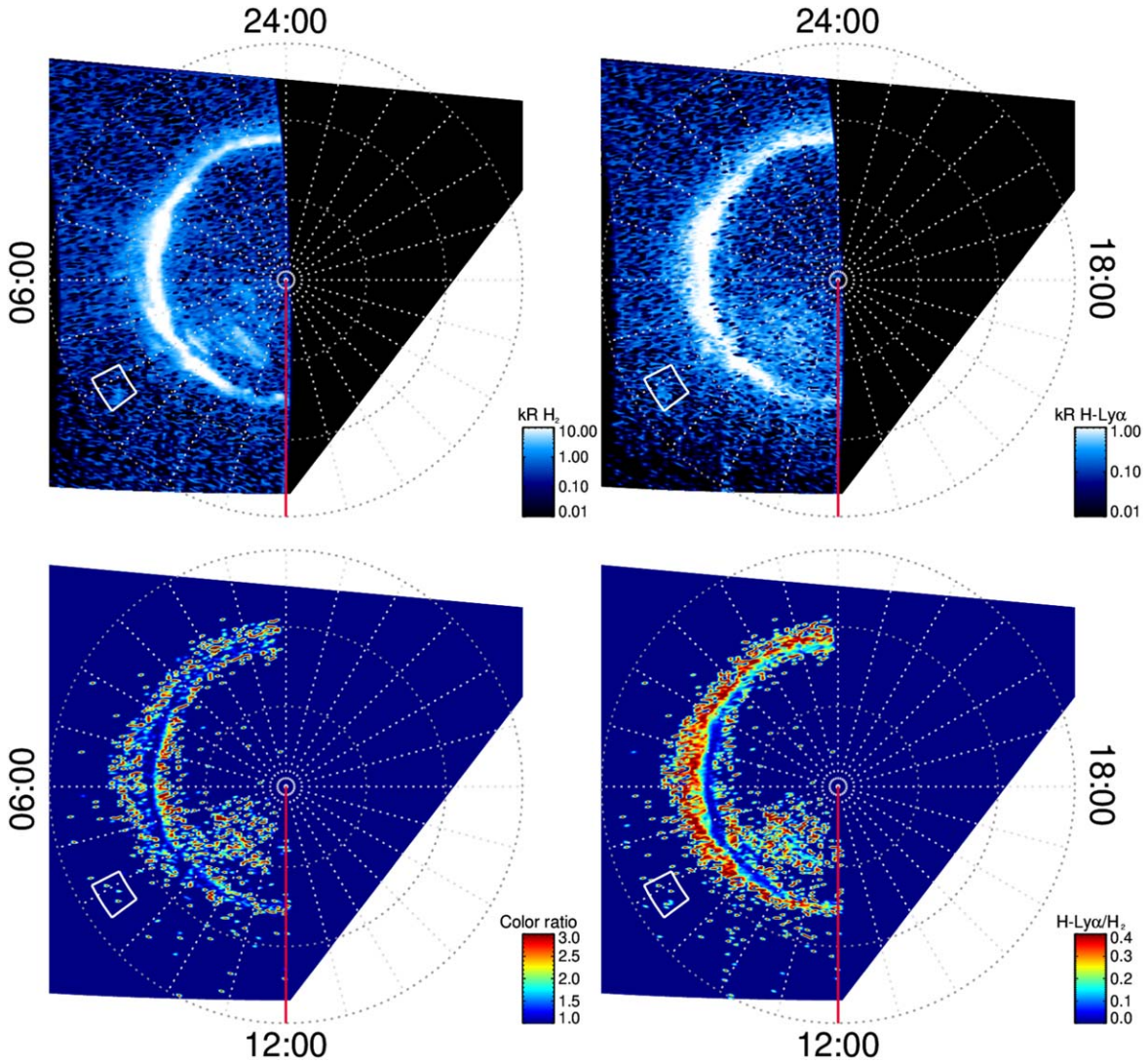

Figure 5. Polar projections of physical observables derived from the UVIS FUV processed observation of 2008 August 26 at 00:53:35. Top left: total H_2 brightness corrected for absorption. Top right: H Lyα brightness corrected for absorption and underlying H_2 contribution. Bottom left: CR. Bottom right: H Lyα/H_2 BR. Duplicated from Magalhães et al. (2019).

the expected footprint, it is difficult to reliably attribute a particular bright spot to a satellite footprint. Magalhães et al. (2019) described an ongoing systematic search for additional footprints in the APIS database of Cassini UVIS and HST Saturn auroral images to better evaluate the detection frequency and set upper brightness limits on the usual nondetections.

UVIS spectra can also be used to assess the mean energy of precipitating electrons. Gustin et al. (2017) examined a large set of Cassini UVIS Saturn auroral spectra and assessed the precipitating primary electron mean energy by two techniques. The CR technique ratios long- and short-wavelength bands in the UVIS FUV spectrum to look for short-wavelength absorption from methane and other hydrocarbons below the homopause. The derived column of hydrocarbon absorbers combined with atmospheric models led to estimates of electron penetration depths consistent with electron mean energies of 7–17 keV. A second technique, better suited for studying spectra with little hydrocarbon absorption, used the ratio of H Lyα/H_2-band emission to find typical electron mean energies of 1–11 keV. Gustin et al. (2017) then applied the H Lyα/H_2-band technique to examine the 2008 spectrum of the Enceladus northern auroral footprint on Saturn (Pryor et al. 2011), which did not show significant hydrocarbon absorption. They found a mean electron energy of 6 keV using an atmospheric model (Koskinen et al. 2015) derived from UVIS occultations for 70°N on Saturn and a mean electron energy of 21 keV using a model derived for 69°S. They suggested the 70° N model was more typical for Saturn, indicating the lower 6 keV primary electron energy estimate is probably preferred.

We also examined spectral information contained in the UVIS FUV data cubes for 2017 September 13–14. Figure 6 compares the summed spectrum of the pre-midnight spot from Image 17 and the post-midnight spot from Image 18 to a laboratory spectrum obtained with the UVIS instrument during its pre-launch calibration, where the spectrum was produced from an electron source impacting molecular hydrogen H_2 gas. Both spectra show molecular band features on both sides of the Lyα line at 121.6 nm and a prominent feature near 158 nm, which we attribute in the Saturn case to auroral-type electrons impacting atmospheric H_2. Also shown is a background spectrum obtained from spatial sectors on each side of the two spatial sectors used in the spot extraction. The background

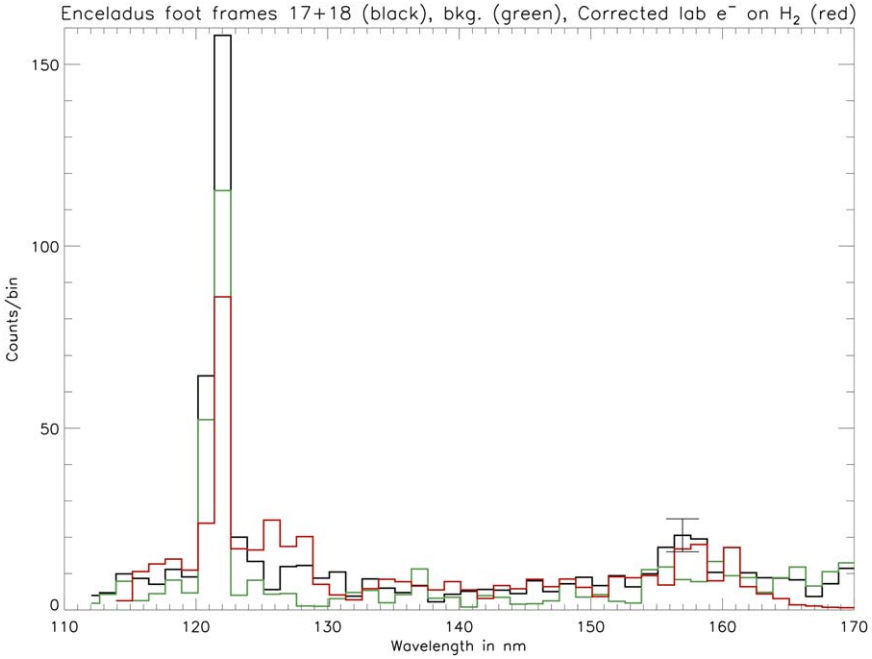

Figure 6. The black line is the sum of two UVIS FUV Enceladus spot spectra of Saturn, from two spatial sectors in image 17 and two spatial sectors in image 18. A 1σ statistical error bar is indicated on the H_2-band feature near 157 nm. The green line is a background measurement extracted from a single spatial sector on each side of each spot. The Saturn spectra have been binned into 64 wavelength channels. No background has been subtracted. The red line is a high-signal-to-noise-ratio UVIS lab spectrum of electrons impacting hydrogen gas, obtained using the full 1024 wavelengths of the detector, rebinned into 64 bins, and corrected for instrument calibration changes since its laboratory calibration.

spectrum does not show obvious H_2 features. The laboratory spectrum has been adjusted for wavelength-dependent instrumental calibration changes between its pre-launch calibration and 2017. The spot spectrum has a low signal-to-noise ratio, but is consistent with electron impact excitation of molecular and atomic hydrogen. Figure 7 compares the background-subtracted, calibrated spectrum of the spot to a nearby patch of bright auroral emission on the main auroral oval obtained in the same spectral image from 2017. The auroral patch has been scaled downward in brightness by a factor of 100 to match the spot spectrum near 160 nm. The spectra roughly agree in shape below 165 nm except at Lyα, where the spot spectrum is relatively brighter, suggesting lower-energy primary electrons, as discussed below.

Here we applied the Lyα/H_2-band technique to the calibrated and background-subtracted spectra obtained in 2017 displayed in Figure 7. The spectra were fit with a multiple linear regression technique, where the two fitting vectors were (1) a Lyα line profile and (2) an H_2 emission band spectra without Lyα emission, previously used by Gustin et al. (2017). The Lyα/H_2 ratio found for the Enceladus spots from images 17 and 18 was $\sim$0.089, much higher than the ratio of $\sim$0.037 found for the auroral patch used in Figure 7. While the interpretation of these ratios is very model-dependent, using the preferred K70N atmospheric model together with the Tao et al. (2014) curve divided by 2 shown in Figure 7(a) of Gustin et al. (2017) indicates these ratios correspond to an Enceladus spot primary electron energy of $\sim$18 keV in 2017 compared to a much higher value of $\sim$60 keV for the corresponding auroral patch. This result for the Enceladus spot energy is somewhat higher in energy than the finding from Gustin et al. (2017) of 6 keV in the K70N model for the Enceladus spot from 2008. However, the very low signal-to-noise ratio on the spot spectrum and the subtraction of a large dayglow background lead to large error bars on the extracted Lyα signal of the spot (Figure 6) and make this only a very rough estimate for the primary electron energy.

We now briefly consider why the spots were observed on this occasion and not on most other opportunities. Variability in the Enceladus plume itself exists, tied to the distance of Enceladus from the planet's center, with the brightest plume activity seen near Enceladus' apocenter (e.g., Hedman et al. 2013; Ingersoll et al. 2020). One can expect a stronger interaction when the plume activity is high because of more collisions/momentum exchange between the plasmas, which can lead to stronger field-aligned currents and a possibly detectable spot. On 2017 September 13, Enceladus was closest to Saturn at 22:10; on 2017 September 14, Enceladus was farthest from Saturn at 14:37. The spots reported here from 2017 September 14 from hours 6 to 10 occurred at an intermediate distance from Saturn and are not obviously linked to the Enceladus range from Saturn, unless there is a time delay involved.

Another possibility to consider is a link between activity on the main auroral oval and the brightness of the Enceladus spot, perhaps due to solar wind compression of the magnetosphere. We note that the time interval containing these 2017 Enceladus footprint detections was well documented by Palmaerts et al. (2018), who studied an auroral brightening event in UVIS data and in Saturn Kilometric Radio (SKR) data corresponding to the time of the Enceladus footprint detections discussed here. Figure 8 compares our spot detections in this paper to the trends in peak EUV auroral emission seen from UVIS and in SKR emission recorded by the Cassini Radio and Plasma Wave Science (RPWS) instrument. A sharp increase in the EUV and SKR emission was seen about the time of the spot detections reported here. Figures 3 and 4 also show the main UV auroral oval expanding and brightening as the spots do. Of the 22 sequential UVIS images in observation AURSLEW001

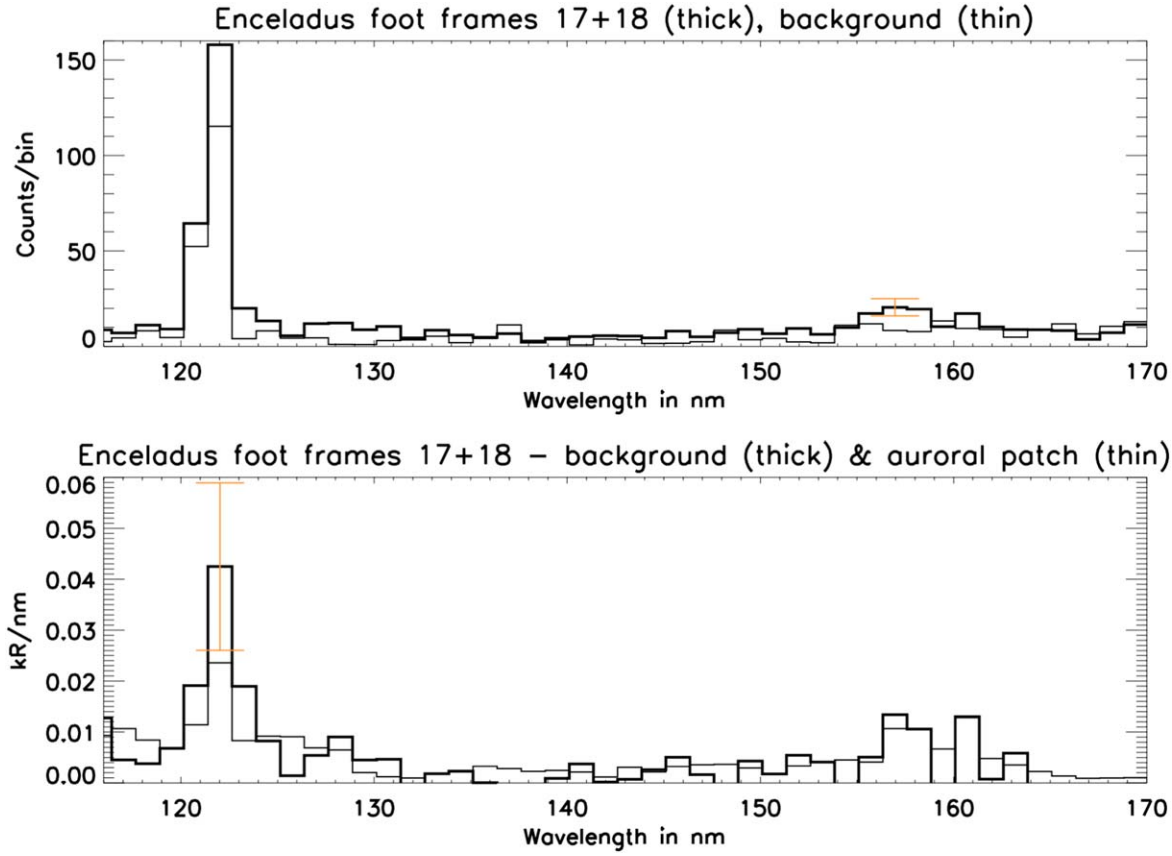

Figure 7. Top panel: this UVIS FUV Saturn spectrum of the Enceladus footprint (thick line) and background are the same as in Figure 6. A 1σ statistical error bar is indicated on the H_2-band feature near 157 nm. Bottom panel: the background has been subtracted from the Enceladus footprint spectrum, and the data have been calibrated. A 1σ statistical error bar is indicated on the Lyα band feature near 121.6 nm. A brighter auroral spectrum (thin line) is shown from the same spectral image, scaled down in brightness by a factor of 118 so that the spectra are normalized near 160 nm.

obtained with 16 s integrations, the first five were obtained with the Enceladus footprint search box out of view. The next nine showed the search box, but lacked an obvious spot. The next three images showed an EUV spot, but no obvious FUV spot (Figure 3). The next two images showed both EUV and FUV spots (Figure 4). The last three images did not show obvious spots, as the main aurora had brightened and expanded too much to make the relatively faint spots visible above the increasing background. We conclude that a plausible reason for the new Enceladus footprint spot detections is a general magnetospheric compression leading to enhanced auroral emissions on the main oval and at the footprint location. It is also true that the 16 s integrations used in this UVIS observing sequence instead of the usual 8 s integrations favored the detection of weak signals. We also looked at the 2008 Enceladus spot detections beginning on 2008 August 26 at 00:53 (early on day of year (DOY) 239) and looked for an SKR enhancement due a magnetospheric compression, and found that there was one beginning near noon on DOY 238 and lasting for several Saturn rotations, supporting the idea that these solar wind events create favorable conditions for Enceladus footprint detections.

In addition to UV footprint data, there is other evidence for activity associated with the Enceladus–Saturn magnetic flux tube. Rymer et al. (2009) and Pryor & Rymer et al. (2011) presented Cassini Magnetospheric Imaging Instrument, Cassini Plasma Spectrometer, and Cassini Magnetometer data from 2008 August 11, showing the presence of field-aligned ion and electron beams approaching Cassini from the north when the spacecraft was 3.6–23.3 Enceladus radii downstream of Enceladus. The electron distributions flickered in mean energy between 10 eV and 1 keV energies. Gurnett et al. (2011) and Gurnett & Pryor (2012) found that auroral hiss emissions were associated with observed field-aligned low-energy electron beams (1–50 eV) and currents seen when Cassini was near Enceladus. The various beams observed near Enceladus may be related to the observed UV spots on Saturn.

More recently, Sulaiman et al. (2018) reported that auroral hiss was seen in Cassini RPWS data on a higher-latitude (53.°2N) near-Saturn crossing of the flux tube linking Enceladus to Saturn on 2017 September 2. They ray-traced the auroral hiss whistler-mode emission to an upward electron beam source near the Enceladus northern auroral footprint on Saturn. They also presented evidence in the concurrent magnetic field data for associated downward and upward currents. Unfortunately, as shown in Figure 9, Cassini was not in the correct longitude or L-shell position during the 2017 September 13–14 Cassini UVIS observations presented here for Cassini RPWS observations to study auroral hiss along the field line linking Enceladus to Saturn. When Cassini did cross the $L = 4$ shell associated with Enceladus on the following day, 2017 September 15, Cassini was separated by more than 100° in longitude from Enceladus. However, previous work suggests that Enceladus-linked auroral hiss associated with low-energy electron beams is usually present, unlike the Enceladus-related UV-bright spots on Saturn discussed here.

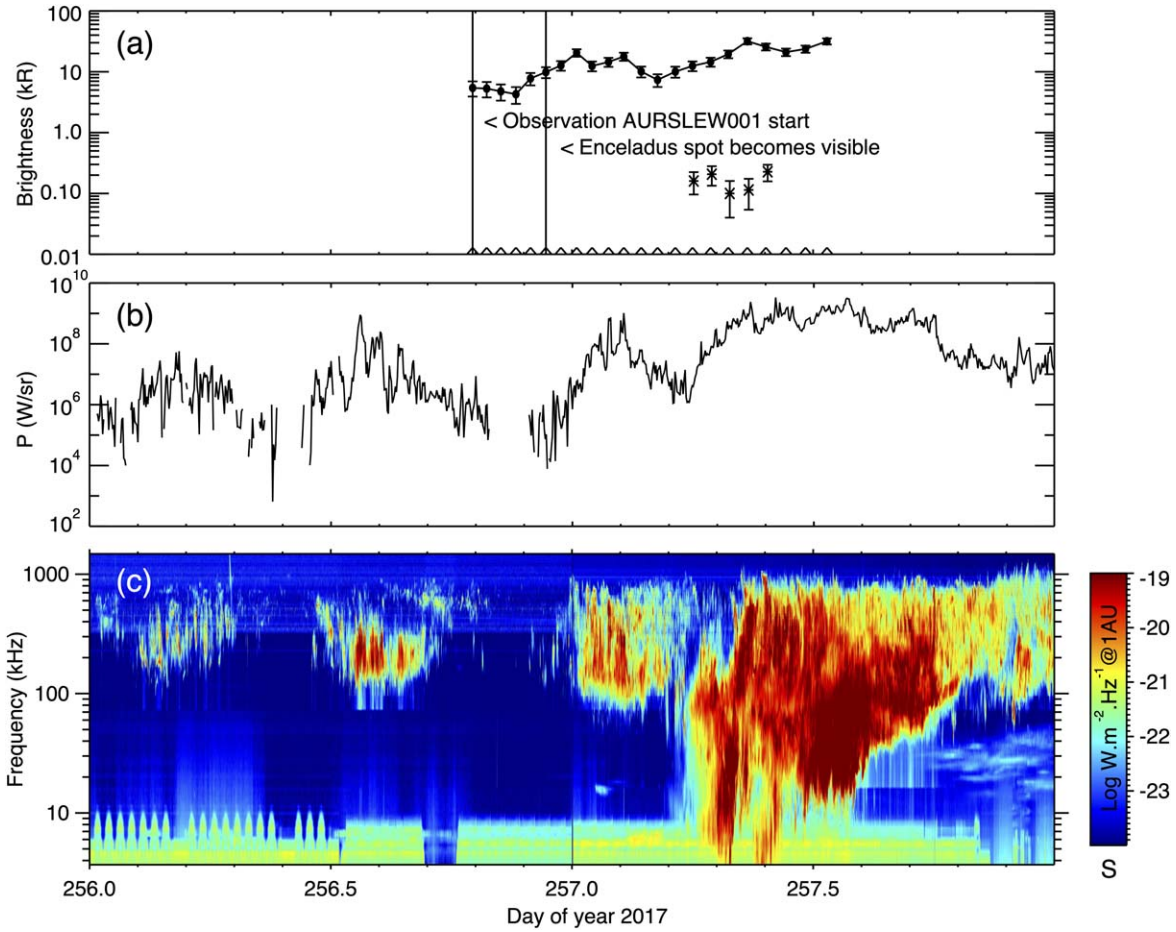

Figure 8. (a) The AURSLEW001 EUV image times are indicated by ∧ symbols. The vertical lines indicate when AURSLEW001 began and when the search box rotated into view and the Enceladus spot became visible, if present. The five actual spot detections are shown with the EUV brightnesses (in kR) and 1σ error bars indicated. The last three images did not have detections, possibly because the main auroral oval had expanded and brightened, increasing the background. Also shown (filled circles) are the peak brightness values in each image due to the main aurora with 5σ error bars. (b) The corresponding SKR power is shown from the Cassini RPWS. (c) The corresponding SKR spectrum is shown from the Cassini RPWS.

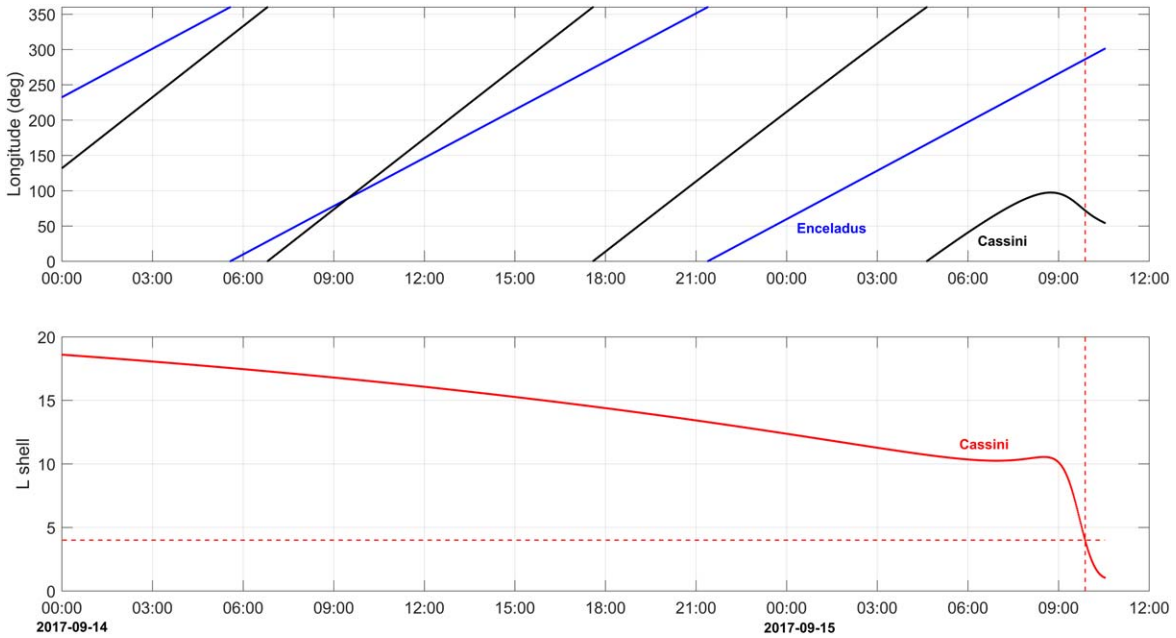

Figure 9. Top panel: the longitudes of Enceladus (in blue) and Cassini (in black) are shown for 2017 September 14–15. Bottom panel: the L-shell values of Cassini (solid line) and Enceladus (dashed line) are shown for 2017 September 14–15.

Theoretical investigations predict an Alfvénic disturbance associated with the magnetosphere rotating past the conducting obstacle formed by Enceladus. Hess et al. (2011) argued that the Alfvén waves produced near Enceladus undergo turbulent filamentation and calculated a precipitating electron power for Enceladus of 10^7–10^8 W, consistent with the power of the previously observed UV footprints, but much lower than the 10^{12} W associated with Io. For their assumed power transfer efficiency from electrons to auroral emissions of 10%, the expected auroral emission at Enceladus would be of order $\sim 10^6$–10^7 W, consistent with emissions from a 1 kR spot the size of the projection of Enceladus' footprint along the field line onto Saturn's atmosphere. This 10% transfer efficiency estimate was recently confirmed in a study of Io–Jupiter coupling using data from the Juno spacecraft (Sulaiman et al. 2023). Hess et al. (2011) also pointed out that for Saturn with its 0° magnetic field tilt, the main Alfvén wave-driven spot from electrons traveling from Enceladus onto Saturn should merge with the transhemispheric electron beam spot from electrons traveling upward from Saturn and traveling to the other hemisphere before traveling downward to Saturn. Saur et al. (2013) calculated the Poynting flux from the Alfvénic disturbance traveling toward Saturn from near Enceladus and found the computed 0.2×10^9 W power was sufficient to explain the observed UV footprints thought to be derived from 1 to 4×10^6 W of power in precipitating electrons.

North–south asymmetries in the Saturn–Enceladus system may be important. So far all of the reported Enceladus-related spots have been in the north, which may be an artifact of the distribution of observations. The Enceladus plumes emerge from the south polar region of Enceladus and provide water molecules that are later ionized to make a plasma torus (e.g., Hansen et al. 2006; Waite et al. 2006). Bonfond (2013) noted that because of the northward offset of Saturn's dipole magnetic field relative to Saturn's center, Enceladus is always located about 10 Enceladus radii, or 0.04 R_S (Saturn radii), south of the center of its associated plasma torus. Simon et al. (2013) calculated Alfvén wave transmission from a near-Enceladus source through the associated torus and found the power transmitted toward the south should be orders of magnitude larger than toward the north. On the other hand, they also noted that Saturn's northern auroras are generally brighter than the southern ones, because of the higher magnetic field in Saturn's north polar region compared to the southern due to the north–south offset of Saturn's dipole field. Still, the overall expectation is that southern Enceladus-related auroral spots on Saturn exist and remain to be identified, perhaps in Cassini UVIS or HST data.

4. Conclusions

We have found that in certain cases UVIS data should be limb-fit before analysis, rather than relying on the JPL-provided geometry kernels. This is particularly true for the data obtained in Rev. 293 at the end of the mission. After limb-fitting, five sequential images from 2017 spanning about 3 hr and 40 minutes were found to have significant excess molecular and atomic hydrogen EUV emission near local midnight at the expected location of the northern Enceladus auroral footprint, with the last two images also showing significant excess FUV emission. The FUV emission spectrum from the last two footprint images was used to estimate a primary electron energy of 18 keV. These new images add to the previously published set of three images of the northern Enceladus auroral footprint from Pryor & Rymer et al. (2011), obtained with slightly more favorable viewing conditions (a larger sub-spacecraft latitude of 74°N–65°N and a closer range to Saturn's center of 8.1–6.0 R_S). Considering that several thousand UVIS auroral images are available and have been inspected, it appears that the Enceladus auroral footprint is usually too dim to be seen by UVIS or simply absent. In the new case, the footprint detections are accompanied by a strong enhancement in the SKR and main auroral oval UV emissions, suggesting the presence of a magnetospheric compression event. Finally, the limited evidence from crossings of the Enceladus flux tube by Cassini suggests electron beams of low-energy electrons are usually present.

Acknowledgments

W.P., L.E., J.G., A.R., and A.S. acknowledge past support from the NASA/JPL Cassini Project. W.P. also acknowledges past support from NASA's Cassini Data Analysis Program (CDAP) and ongoing support from Central Arizona College. French coauthors were supported by CNES and CNRS/INSU national programs of planetology (PNP) and heliophysics (PNST).

ORCID iDs

Wayne R. Pryor https://orcid.org/0000-0001-8112-8783
Abigail M. Rymer https://orcid.org/0000-0002-4879-0748
Ali H. Sulaiman https://orcid.org/0000-0002-0971-5016

References

Bader, A., Cowley, S. W. H., Badman, S. V., et al. 2020, GeoRL, 47, e85800
Bonfond, B. 2013, in Geophys. Monogr. Ser 197, Auroral Phenomenology and Magnetospheric Processes: Earth and Other Planets, ed. A. Keiling et al. (Washington, DC: AGU), 133
Bonfond, B., Gladstone, G. R., Grodent, D., et al. 2017, GeoRL, 44, 4463
Clarke, J. T., Ajello, J., Ballester, G., et al. 2002, Natur, 415, 997
Connerney, J. E. P., Baron, R., Satoh, T., et al. 1993, Sci, 262, 1035
Esposito, L. W., Barth, C. A., Colwell, J. E., et al. 2004, SSRv, 115, 299
Esposito, L. W., Colwell, J. E., Larsen, K., et al. 2005, Sci, 307, 1251
Gérard, J.-C., Bonfond, B., Gustin, J., et al. 2009, GeoRL, 36, L02202
Grodent, D., Gustin, J., Gérard, J.-C., et al. 2011, JGR, 116, A09225
Gurnett, D. A., Averkamp, T. F., Schippers, P., et al. 2011, GeoRL, 38, L06102
Gurnett, D. A., & Pryor, W. R. 2012, in Geophys. Monogr. Ser 197, Auroral Phenomenology and Magnetospheric Processes: Earth and Other Planets, ed. A. Keiling et al. (Washington, DC: AGU), 305
Gustin, J., Grodent, D., Radioti, A., et al. 2017, Icar, 284, 264
Gustin, J., Stewart, I., Gérard, J.-C., & Esposito, L. 2010, Icar, 210, 270
Hansen, C. J., Esposito, L., Stewart, A. I. F., et al. 2006, Sci, 311, 1422
Hedman, M. M., Gosmeyer, C. M., Nicholson, P. D., et al. 2013, Natur, 500, 182
Hess, S. L. G., Delamere, P. A., Dols, V., et al. 2011, JGRA, 116, A01202
Ingersoll, A. P., Ewald, S. P., & Trumbo, S. K. 2020, Icar, 344, 113345
Koskinen, T. T., Sandel, B. R., Yelle, R. V., et al. 2015, Icar, 260, 174
Lamy, L., Magalhães, F., & Henry, F. 2021, APIS/Cassini/UVIS Data Collection (Version 1.0). PADC
Lamy, L., Prangé, R., Henry, F., & Le Sidaner, P. 2015, A&C, 11, 138
Lamy, L., Prangé, R., Pryor, W., et al. 2013, JGRA, 118, 4817
Lamy, L., Prangé, R., Tao, C., et al. 2018, GeoRL, 45, 9353
Magalhães, F. P., Lamy, L., & Prangé, R. 2019, AGUFM, SM33F–3271
McClintock, W. E. 2002, Cassini UVIS Calibration Report, Draft 2.2., https://studylib.net/doc/12631315/calibration-report-cassini-uvis-draft-2.2
Mura, A., Adriani, A., Connerney, J. E. P., et al. 2018, Sci, 361, 774
Palmaerts, B., Radioti, A., Grodent, D., et al. 2018, GeoRL, 45, 6832
Prangé, R., Rego, D., Southwood, D., et al. 1996, Natur, 379, 323
Pryor, W. R., Esposito, L. W., Jouchoux, A., et al. 2019, JGRE, 124, 1979
Pryor, W. R., Rymer, A. M., Mitchell, D. G., et al. 2011, Natur, 472, 331
Radioti, A., Yao, Z., Grodent, D., et al. 2019, ApJL, 885, L16
Rymer, A. M., Mitchell, D. G., Hill, T. W., et al. 2009, AGUSM, P32A–06

Saur, J., Grambusch, T., Duling, S., et al. 2013, A&A, 552, A119
Simon, S., Kriegel, H., Saur, J., et al. 2013, JGRA, 118, 3430
Sulaiman, A. H., Kurth, W. S., Hospodarsky, G. B., et al. 2018, GeoRL, 45, 7347
Sulaiman, A. H., Szalay, J. R., Clark, G., et al. 2023, GeoRL, 50, e2023GL103456
Tao, C., Lamy, L., & Prange, R. 2014, GeoRL, 41, 6644
Villanueva, G. L., Hammel, H. B., Milam, S. N., et al. 2023, NatAs, 7, 1056
Waite, J. H., Combi, M. R., Ip, W.-H., et al. 2006, Sci, 311, 1419
Wannawichian, S., Clarke, J. T., & Pontius, D. H. 2008, JGRA, 113, A07217